ARTICLE

Check for updates

Reactions of CO_2 and ethane enable CO bond insertion for production of C3 oxygenates

Zhenhua Xie[1,2,8], Yuanguo Xu[2,3,8], Meng Xie[2,4,8], Xiaobo Chen[5], Ji Hoon Lee[2], Eli Stavitski[6], Shyam Kattel [7✉] & Jingguang G. Chen [1,2✉]

Reacting CO_2 and ethane to synthesize value-added oxygenate molecules represents opportunities to simultaneously reduce CO_2 emissions and upgrade underutilized ethane in shale gas. Herein, we propose a strategy to produce C3 oxygenates using a tandem reactor. This strategy is achieved with a Fe_3Ni_1/CeO_2 catalyst (first reactor at 600–800 °C) for CO_2-assisted dehydrogenation and reforming of ethane to produce ethylene, CO, and H_2, and a $RhCo_x/MCM$-41 catalyst (second reactor at 200 °C) enabling CO insertion for the production of C3 oxygenates (propanal and 1-propanol) via the heterogeneous hydroformylation reaction at ambient pressure. In-situ characterization using synchrotron spectroscopies and density functional theory (DFT) calculations reveal the effect of Rh–Co bimetallic formation in facilitating the production of C3 oxygenates. The proposed strategy provides an opportunity for upgrading light alkanes in shale gas by reacting with CO_2 to produce aldehydes and alcohols.

[1] Chemistry Division, Brookhaven National Laboratory, Upton, NY 11973, USA. [2] Department of Chemical Engineering, Columbia University, New York, NY 10027, USA. [3] School of Chemistry and Chemical Engineering, Jiangsu University, Zhenjiang 212013, China. [4] School of Pharmacy, Jiangsu University, Zhenjiang 212013, China. [5] Department of Mechanical Engineering, State University of New York at Binghamton, NY 13902, USA. [6] National Synchrotron Light Source-II, Brookhaven National Laboratory, Upton, NY 11973, USA. [7] Department of Physics, Florida A&M University, Tallahassee, FL 32307, USA. [8] These authors contributed equally: Zhenhua Xie, Yuanguo Xu, Meng Xie. ✉email: shyam.kattel@famu.edu; jgchen@columbia.edu

In recent decades, increasing anthropogenic CO_2 emissions[1–3] and verified huge shale gas reserves[4,5] have led to studies of effective ways of utilizing these molecules for synthesis of value-added chemicals. The catalytic reduction of CO_2 by light alkanes (methane, ethane, propane, etc.) has been the subject of many investigations due to its promising role in mitigating CO_2 emissions and producing chemical intermediates, such as syngas $(CO + H_2)$[6–11], alkenes[9,10,12,13], and aromatics[13,14]. However, there is a lack of feasible strategy to produce oxygenates directly from CO_2 and shale gas. Oxygenates (e.g., aldehyde and alcohol) are important chemicals and feedstocks widely used in the automotive, fine chemical, and pharmaceutical industries[15,16]. Thus, it is highly appealing to develop an effective strategy that enables the production of oxygenates by directly inserting CO moiety from CO_2 into alkenes generated from shale gas.

Traditional hydroformylation, known as an important oxo-synthesis route[17–19], could be used as an important bridge to achieve the production of oxygenates from CO_2 and shale gas. It involves the addition of syngas to alkenes to produce aldehydes and/or alcohols with 100% atom efficiency[20]. Syngas can be derived from natural gas, naphtha, or coal by partial oxidation or steam reforming[21,22]. Alkenes are typically produced from the partially oxidative cracking of naphtha or alkanes[23,24]. However, the transportation and storage of the highly toxic syngas and flammable alkenes raise potential safety risks[21,22]. Such drawbacks of the traditional hydroformylation process could be avoided if the feedstocks (alkenes and syngas) produced from the upstream reactor can be directly used for the downstream hydroformylation reaction, i.e., the tandem reactor strategy as shown in Fig. 1.

It has been identified that the catalytic reduction of CO_2 by ethane (the second most abundant component in shale gas) can proceed with either dry reforming (via C–C bond cleavage) to generate syngas or oxidative dehydrogenation (via C–H bond cleavage) to yield ethylene[11]. Depending on catalyst properties and reaction conditions, the ratio of ethylene/syngas could be tuned[6], making it possible to use the product mixture as reactants to produce C3 oxygenates (propanal and 1-propanol) from CO_2 and ethane via the strategy illustrated in Fig. 1.

Compared with the traditional high-pressure homogenous hydroformylation, the proposed strategy would benefit by carrying out reactions at ambient pressure, as illustrated by the thermodynamic analysis of C3 oxygenates at different pressures in Supplementary Fig. 1. This in turn requires efficient heterogeneous catalysts for both reactions to promote the formation of C3 oxygenates. Non-precious FeNi/CeO_2 catalyst is a good candidate for step (I) due to its role in readily tuning ethylene/syngas ratio using Fe_x/Ni_y catalysts with different stoichiometries[6]. Different from the ligand complexes used in the traditional homogeneous hydroformylation catalysis, supported metal catalysts should be used for the heterogeneous reaction in step (II). Several previous studies have revealed that Rh, Co, and their bimetallic are the most promising catalysts[21,22,25,26]. However, it is not clear how these catalysts would perform in the tandem configuration

with the hydroformylation feeds being directly generated from the reaction of CO_2 and ethane.

In the present work, we explore the possibility of achieving the strategy to produce C3 oxygenates from CO_2 and ethane. The experimental conditions are first identified using thermodynamic analyses for promising equilibrium conversions of CO_2 and ethane into C3 oxygenates. Then, experiments with a tandem reactor validate the feasibility of the proposed reaction strategy using the combination of Fe_3Ni_1/CeO_2 and Rh-based catalysts supported on a high surface area MCM-41 substrate. Finally, in-situ characterizations and density functional theory (DFT) calculations unravel the role of Co species in modifying the structural and electric properties of Rh, enhancing the formation of C3 oxygenates.

Results

Thermodynamic analyses of reactions at ambient pressure. Figure 2a shows that the direct conversion of ethane and CO_2 into propanal is unfavorable with a highly positive ΔG^0 (purple line). However, it could be achieved using an alternative strategy as shown in Fig. 1 by dividing the overall reaction into two cascade steps: (I) production of ethylene and syngas and (II) subsequent hydroformylation. Figure 2a also shows that both dehydrogenation (blue and black lines) and reforming (red line) of ethane are favorable at high temperatures. In contrast, the hydroformylation of ethylene (golden line) thermodynamically prefers to occur at low temperatures. As a result, there is a thermodynamic gap between steps (I) and (II), which can be bridged using a tandem reactor to run each step within respective favorable temperature regions. To explore the feasibility of this hypothesis, equilibrium analyses were carried out at atmospheric pressure at different temperatures. As illustrated in Fig. 2b, the equilibrium distribution of products strongly depends on the temperature of the first reactor ($C_2H_6 + CO_2$): syngas is the dominant product below 600 °C, whereas C_2H_4 becomes comparable with syngas at above 700 °C. Subsequently, the equilibrium products (mainly CO, H_2, and C_2H_4) from the first reactor obtained at different temperatures are used as the feed for the hydroformylation reaction in the second reactor (200 °C). Figure 2c shows that the second reactor can yield 7–55% of oxygenates (propanal and 1-propanol) as the first reactor (feed ratio of C_2H_6/CO_2 = 1 mol/0.5 mol) is maintained from 600 °C to 1000 °C.

Catalytic performance tests with single and tandem reactors. Based on the thermodynamic analyses, flow reactor experiments were performed using a tandem reactor configuration: first reactor (600–850 °C) loaded with Fe_3Ni_1/CeO_2; second reactor (200 °C) loaded with Rh-based catalysts. Figure 3a shows that distributions of C_2H_4, CO, and H_2 from the first reactor strongly depended on the temperature. Below 700 °C, the production of C_2H_4 was negligible compared with that of syngas. At 750 °C and above, the C_2H_4/CO/H_2 ratio approached to a typical hydroformylation feed ratio (1 : 1 : 1). As for the second reactor, using pure feed of C_2H_4, CO, and H_2, Fig. 3b and Supplementary Table 2 illustrate that as the Co/Rh bimetallic ratio increased, the yield of oxygenates increased from 2.4% on Rh/MCM-41 to 13.2% and 16.9% on Rh_1Co_1/MCM-41 and Rh_1Co_3/MCM-41, respectively. Moreover, the selectivity of 1-propanol also increased and even became comparable with propanal (15.8% vs. 16.5%) on Rh_1Co_3/MCM-41, offering a way to control the alcohol/aldehyde ratio. In addition, the oxygenate selectivity could also be affected by temperature that 42.5% of propanal was obtained on Rh_1Co_3/MCM-41 at 180 °C (denoted as Rh_1Co_3* in Fig. 3b). As indicated by the Supplementary Table 2 and
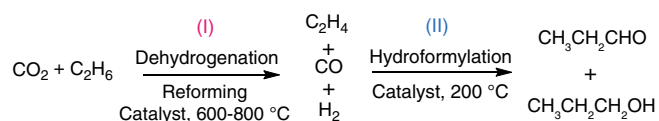

Fig. 1 Reaction scheme of the production of C3 oxygenates from the upgrading of CO_2 and ethane. Ethylene and syngas are produced from the first reactor via the CO_2-assisted dehydrogenation and reforming of ethane and subsequently used for the hydroformylation reaction in the second reactor to produce propanal and/or 1-propanol.
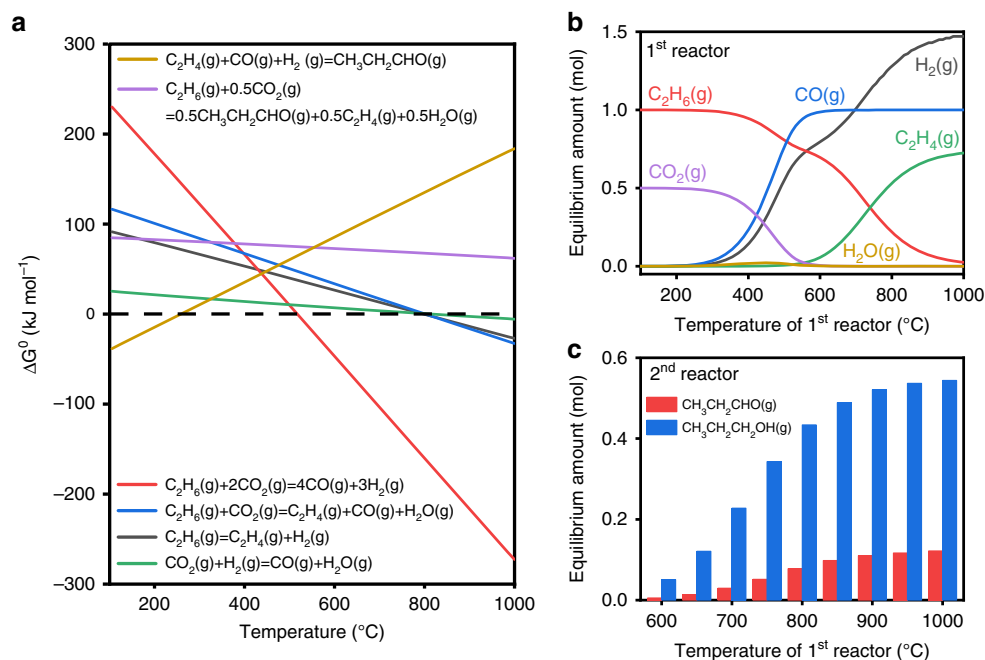
Fig. 2 Thermodynamic analyses of the proposed reaction strategy at the atmospheric pressure. a Diagram of standard Gibbs free energy change (ΔG^0) of involving reactions along with temperature. **b** Equilibrium species distribution as a function of temperature within the first reactor (feed ratio of C_2H_6/ $CO_2 = 1$ mol/0.5 mol). **c** Equilibrium amount of C3 oxygenates (propanal and 1-propanol) formed at 200 °C within the second reactor using the products of the first reactor, which is maintained within the temperature range of 600–1000 °C. All the thermodynamics were calculated with HSC Chemistry 6.0.

Supplementary Figs. 3–6, the measured propanal/1-propanol ratios in the second reactor were above 1.0, higher than the equilibrium ratio of 0.26 at 200 °C (Supplementary Fig. 15), indicating that the interconversion between propanal and 1-propanol did not reach equilibrium. For the tandem reactor configuration in Fig. 3c, C3 oxygenates were detected on the Rh_1Co_x/MCM-41 catalysts as the first reactor ran at above 600 °C. Control experiments with MCM-41, quartz sand, and blank tubing exhibited negligible oxygenates production (Supplementary Table 2–4). The highest yield of C3 oxygenates (~4.7%) was achieved by using the Fe_3Ni_1/CeO_2 (at 800 °C) and Rh_1Co_3/MCM-41 (at 200 °C) catalysts. As shown in Supplementary Fig. 7, a further increase in the C3 oxygenate yield toward 7.2% could be achieved by increasing the catalyst loading and modifying the reaction conditions. In addition, the durability of the Fe_3Ni_1/CeO_2 catalyst, within the testing period of 31 h (Supplementary Fig. 8), indicated a stable feed supply for the downstream reactor. These results validate the feasibility of using the tandem reactor configuration to convert CO_2 and ethane into C3 oxygenates.

It is noted that the values for conversion, turnover frequency (TOF), and oxygenates yield (Supplementary Figs. 2–6 and Supplementary Table 2) over Rh_1Co_3/MCM-41 were higher than the sum of that of Rh/MCM-41 and Co_3/MCM-41, indicating a synergistic effect between Rh and Co in the bimetallic catalysts. To elucidate the origin of such effect, the metal particle size distributions were obtained based on the high-angle annular dark-field (HAADF) images shown in Supplementary Figs. 9–11. Elemental mappings in Supplementary Figs. 10 and 11 indicated a uniform distribution of Co around Rh particles. As the Co/Rh ratio increased from 0:1 to 1:1 and 3:1, metal particle size decreased from ~2.3 nm to ~1.7 nm and ~1.4 nm with a narrower distribution. The CO uptake values also increased from 57.6 µmol g^{-1} on Rh/MCM-41 to 78.9 and 108.1 µmol g^{-1} on Rh_1Co_1/MCM-41 and Rh_1Co_3/MCM-41, respectively. Thus, the presence of Co promoted the dispersion of the Rh particles.

In-situ X-ray absorption fine structure analysis. In-situ X-ray absorption near edge structure (XANES) and extended X-ray absorption fine structure (EXAFS) spectra of Rh K-edge and Co K-edge were measured to explore the electronic properties and local environments under hydroformylation conditions. Referring to the XANES spectra of metal and oxides standards in Fig. 4a, Rh in Rh/MCM-41 was slightly oxidized and it became more oxidized with the presence of Co. As shown in Fig. 4c, the EXAFS signals in R space indeed showed a significant peak located between 1.5–2.0 Å, correlating with the coordination by low-Z elements (e.g., C or O). It is difficult to distinguish the contributions from Rh–C or Rh–O bonds due to their similar bond length. The possibility of Rh–O bond from bulk Rh oxides could be ruled out due to the lack of corresponding Rh–Rh peaks from bulk oxides. Nevertheless, given the fine assembles from HAADF images, a Rh–O contribution from the MCM-41 substrate could not be excluded. Temperature-programmed reduction (TPR) profiles on both the mono- and bimetallic Rh-based catalysts show that besides the reduction of bulk Rh oxides at 100–110 °C, a peak located within 275–285 °C was observed. The latter should correlate with the reduction of the Rh species interacted with the silica framework (Supplementary Fig. 12). Rh–C interaction, especially from CO adsorption, could also be possible due to the formation of carbonyl on the Rh surface[27,28]. Thus, the Rh-low Z peak was assigned to both of Rh–C and Rh–O contributions. The peak located between 2.0 Å and 3.0 Å was mainly associated with the Rh–M (Rh or Co) bonds. With increasing Co/Rh ratio from 0:1 to 1:1 and 3:1, the Rh–M peak noticeably decreased, validating the reduction of Rh particle size as suggested by the transmission electron microscopy (TEM) and CO chemisorption experiments. In Fig. 4b, the Co K-edge spectrum of Co_3/MCM-41 showed a strong white line due to the strong interaction between Co^{2+} and silica framework[29]. As shown in Fig. 4d, nearly negligible Co–Co bond from bulk oxides was observed on the bimetallic samples, suggesting that the majority of the Co species was highly dispersed on the MCM-41 support. However, it is
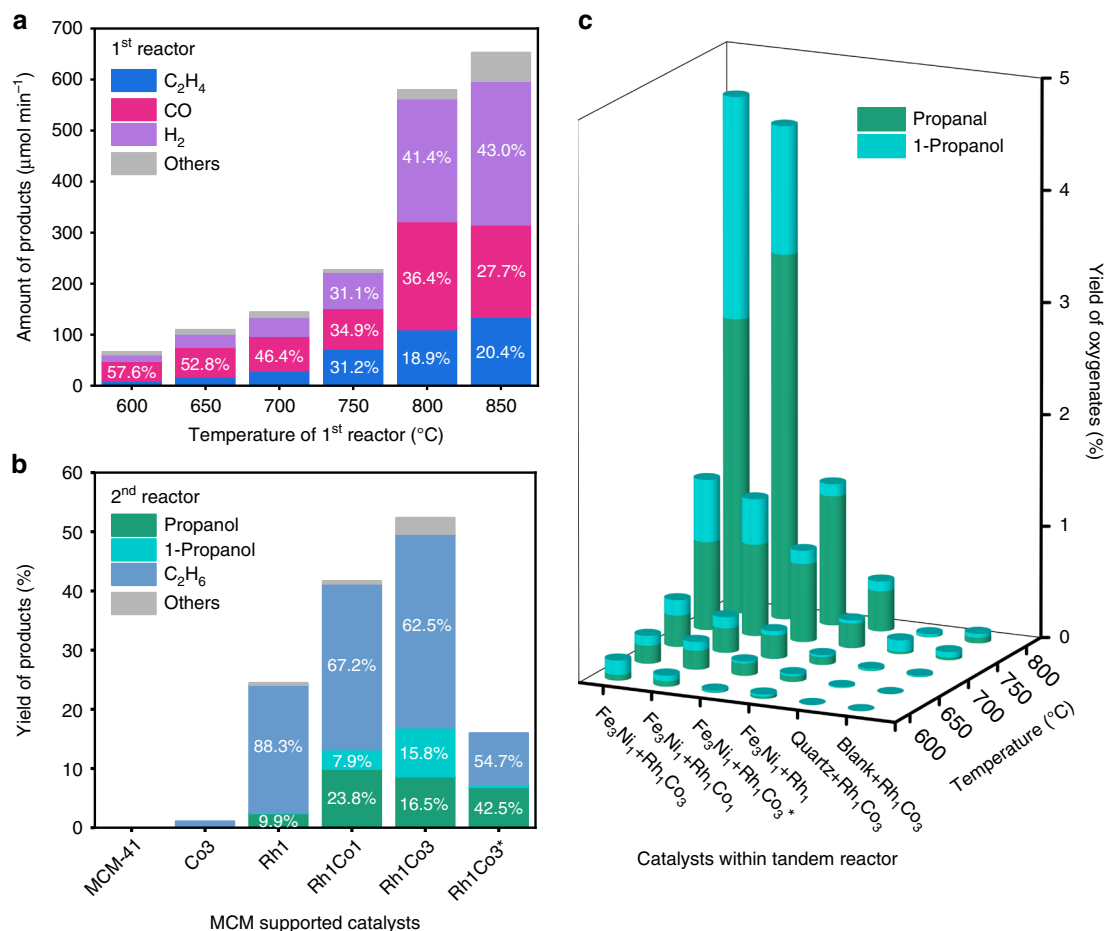
Fig. 3 Catalytic performance of different catalysts. a Amount of products formed during the reaction of CO_2 and C_2H_6 over Fe_3Ni_1/CeO_2 at different temperatures (600–850 °C). **b** Product yield (C_2H_4-based) of the reaction of C_2H_4, CO, and H_2 over the MCM-41 supported Rh-based catalysts at 200 °C. **c** Product yield (C_2H_6-based) of the reaction of CO_2 and C_2H_6 within the tandem reactor (first reactor: 600–800 °C, second reactor: 200 °C). Note: the numbers within the bars of Fig. 3a, b indicate product selectivity.

noted that the bimetallic samples showed an even stronger white line, indicating a decrease of electron density at the Fermi level that should result in weak or negligible CO adsorption. Therefore, the majority of Co species that strongly interacted with the silica framework[29] was probably not involved in catalysis. However, given the HAADF and CO chemisorption results, the interaction of CoO_x species with Rh was most likely responsible for the increase of Rh dispersion. $Rh_1Co_1/MCM-41$ and $Rh_1Co_3/MCM-41$ exhibited much higher formation rate of C3 oxygenates (1.12 min^{-1} and 1.04 min^{-1}, respectively) than Rh/MCM-41 (0.26 min^{-1}) by a factor of 4–5 times. Such increase cannot be explained solely by the increase in Rh dispersion (1.4–1.9 times). Moreover, the 1-propanol selectivity also increased with the Co/Rh ratio. It is noted that the EXAFS fitting results of both Rh and Co edges (Supplementary Table 10) indicated the presence of Rh–Co bond on the bimetallic samples. Thus, the increase of the total C3 formation rate and 1-propanol selectivity with the Co/Rh ratio most likely resulted from the fraction of Co that formed bimetallic bond with Rh. To validate this hypothesis, DFT calculations were performed on the Rh and RhCo surfaces as follows.

Density functional theory calculations. The enthalpy change for ethylene hydroformylation to propanal and 1-propanol along the reaction pathways shown in Fig. 5 were calculated on Rh(111) and bulk-terminated-Co_3Rh(111) [Co_3Rh(111) hereafter]

surfaces. The binding energies of involved reaction intermediates at their optimized configurations (Supplementary Fig. 13) were calculated (Supplementary Table 11) to compute the enthalpy change (ΔE) for the formation of propanal and 1-propanol on the two surfaces. The DFT calculated ΔE values along the reaction pathways as illustrated in Fig. 5 showed that the presence of Co on the RhCo bimetallic surface facilitated the formation of 1-propanol due to stronger binding of oxygenate intermediates such as $^*CH_3CH_2CHO$ and $^*CH_3CH_2CH_2O$ compared with Rh(111). Thus, a RhCo bimetallic catalyst with abundant surface Co sites should be expected to show higher selectivity toward 1-propanol formation in the hydroformylation reaction of C_2H_4.

Further DFT calculations were performed to determine the reaction energy (ΔE) and activation energy (E_a) of selected steps for the formation of propanal and 1-propanol. The DFT calculated ΔE and E_a for the first hydrogenation step to form $^*CH_3CH_2$ were (0.33 and 0.77 eV) and (0.42 and 0.68 eV) on Rh(111) and Co_3Rh (111), respectively. The ΔE and E_a values for the second hydrogenation reaction to form propanal ($^*CH_3CH_2CHO$) after the formation of $^*CH_3CH_2CO$ via inserting $^*CO$ into $^*CH_3CH_2$ were (0.59 and 0.82 eV) and (0.31 and 0.46 eV) on Rh(111) and Co_3Rh(111), respectively. The hydrogenation of propanal ($^*CH_3CH_2CHO + ^*H \rightarrow ^*CH_3CH_2CH_2O + ^*$) had ΔE and E_a values of (0.04 and 0.55 eV) and (−0.29 and 0.41 eV) on Rh(111) and Co_3Rh(111), respectively. It was noted that the calculated E_a values for the hydrogenation reactions along reaction pathways were lower on Co_3Rh(111) compared with Rh(111). Thus, the
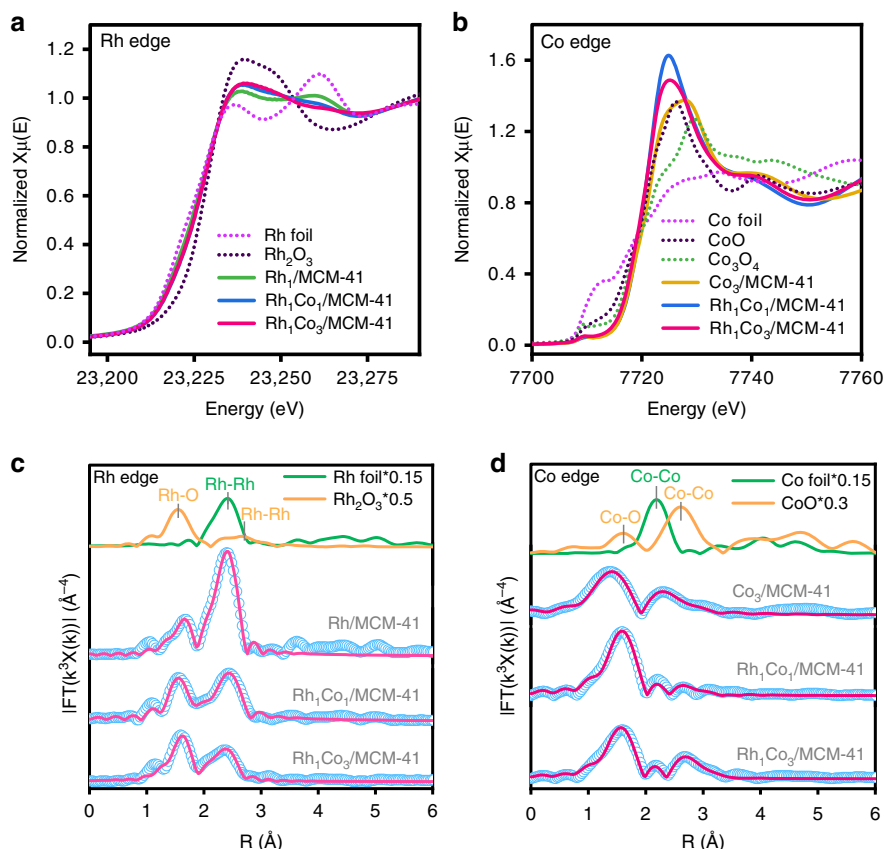
Fig. 4 Structural analyses of mono- and bimetallic MCM-supported Rh-based catalysts. a, **b** XANES spectra of Rh and Co K-edges. **c**, **d** Fourier transformed EXAFS spectra (sky blue circles) and fittings (deep pink line) of Rh and Co K-edges.
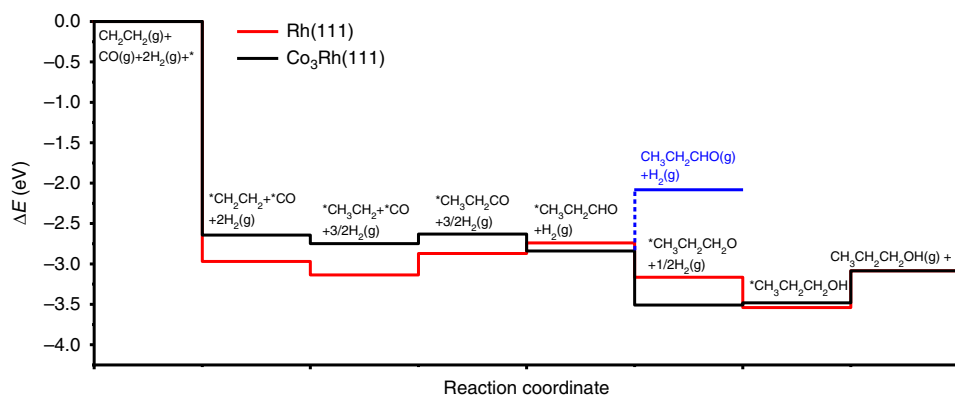

Fig. 5 DFT calculations of reaction pathways on Rh(111) and Co$_3$Rh(111). DFT calculated energy change (ΔE) for hydroformylation into propanal and further hydrogenation into 1-propanol on monometallic Rh and bimetallic RhCo surfaces.

DFT results suggested that hydrogenation of the hydroformylation intermediates was promoted due to the presence of Co on the bimetallic surface. On Rh(111), the desorption of $^*CH_3CH_2CHO$ was uphill by 0.66 eV (blue line) and its hydrogenation to $^*CH_3CH_2CH_2O$ had an E_a of 0.55 eV, thus competing with each other. However, the entropy contribution made desorption more favorable leading to the formation of $^*CH_3CH_2CHO$ as the major product on Rh(111). In contrast, on Co$_3$Rh(111), $^*CH_3CH_2CHO$ desorption was uphill by 0.76 eV and its hydrogenation to $^*CH_3CH_2CH_2O$ had an E_a of 0.41 eV. This showed that the formation of $^*CH_3CH_2CH_2O$, a critical intermediate for 1-propanol formation, was more favorable on Co$_3$Rh(111) compared to Rh(111) due to stronger bindings of $^*CH_3CH_2CHO$ and $^*CH_3CH_2CH_2O$ on Co$_3$Rh(111). The hydrogenation of

$^*CH_3CH_2CH_2O$ to $^*CH_3CH_2CH_2OH$ had ΔE of 0.63 eV and a relatively high E_a of 1.42 eV on Co$_3$Rh(111), indicating that this step was potentially rate-limiting to form 1-propanol. Overall, in agreement with the experimental results, DFT calculations predicted an enhanced production of C3 oxygenates, especially 1-propanol on the Rh–Co bimetallic catalysts.

Discussion

In summary, we have proposed and demonstrated a successful oxygenate production strategy enabled by inserting CO$_2$-derived CO into ethane-derived ethylene using a tandem reactor (with Fe$_3$Ni$_1$/CeO$_2$ and RhCo$_x$/MCM-41 catalysts) at ambient pressure. The presence of Co species could not only promote oxo-synthesis activity by increasing Rh dispersion, but also promote C3

oxygenates formation especially 1-propanol due to favorable hydrogenation of hydroformylation intermediates on the Rh–Co bimetallic surface. This study offers a promising way to simultaneously convert CO_2 and light alkanes in shale gas into value-added aldehydes and alcohols.

Methods

Preparation of Rh-based mono- and bimetallic catalysts. All regents were used without purification. Unless otherwise noted, all of the chemicals ($Fe(NO_3)_3 \cdot 9H_2O$, $Ni(NO_3)_2 \cdot 6H_2O$, $Co(NO_3)_2 \cdot 6H_2O$, $Rh(NO_3)_3 \cdot xH_2O$, CeO_2, and MCM-41) were purchased from Sigma Aldrich. The information of precursors, loading amount and atomic ratio were listed in Supplementary Table 1. All the catalysts were synthesized using an incipient wetness co-impregnation method over the CeO_2 or MCM-41 supports with an aqueous solution of the respective metal precursors. All the catalysts were dried at 80 °C overnight and then calcined at 290 °C for 2 h with a heating ramp rate of 0.8 °C min^{-1}.

Characterization of catalysts. Pulse CO chemisorption was performed in an AMI-300ip (Altamira) instrument. As-prepared catalyst (~100 mg) was pretreated under He atmosphere (50 ml min^{-1}) at 120 °C for 30 min and then cooled to 30 °C. Then, the sample was heated to 200 °C (10 °C min^{-1}) and held for 1 h in a mixture of 10% H_2 in Ar (totally 50 ml min^{-1}), and cooled down in He (50 ml min^{-1}) for degassing before pulsing 10% CO in He (590 μL loop). The amount of chemisorbed CO was used to estimate the number of metal active sites on the catalyst with an assumption of CO/metal ratio being 1 : 1.

The same AMI-300ip (Altamira) instrument was used for TPR measurements. For TPR tests, as-prepared sample (~100 mg) was pretreated under He atmosphere (50 ml min^{-1}) at 120 °C for 30 min and then cooled to 40 °C. TPR test was subsequently performed in a mixture of 10% H_2 in Ar (total 50 ml min^{-1}) with a heating rate of 10 °C min^{-1} to 450 °C. A thermal conductivity detector (TCD) was used to record the hydrogen consumption profile as a function of reduction temperature, allowing a quantitative comparison of the reducibility of active metals in different catalysts.

Metal particle distribution on the spent Rh-based catalysts was characterized using HAADF imaging within an FEI Talos F200X TEM (operated at 200 keV). Scanning TEM–energy dispersive spectroscopy mapping was performed using the same instrument. Spent samples were ultrasonically dispersed in ethanol for 10 min. Afterwards, a droplet was dripped onto lacey carbon film supported on copper grid and fully dried before use.

The in-situ XAFS experiments were carried out at beamline 8-ID (ISS) of the National Synchrotron Light Source II at Brookhaven National Laboratory. The in-situ Rh K-edge (23,220 eV) and Co K-edge (7709 eV) XAFS spectra were collected for MCM-41 supported catalysts, as well as metal foils (Rh and Co) and metal oxide standards (Rh_2O_3, Co_3O_4, and CoO). Approximately 100 mg of sample (60 − 80 mesh) was loaded into a home-designed in-situ copper micro-channel reactor[6]. Graphite carbon paper was used as the reactor window material for transmission and fluorescence modes. Quartz wool was packed at both sides of the sample to fix the catalyst bed. The sample was exposed to the reaction stream (C_2H_4/CO/H_2/He = 3/3/3/3 ml min^{-1}) at 200 °C for 60 min. To reduce thermal disordering contribution, the catalyst bed was cooled to room temperature under the reaction stream. About 30 scans were collected and merged as an individual spectrum to improve the signal-to-noise ratio. Between two scans, an interval time of 45 s was imposed for rest to reduce sample damage potentially induced by the high-flux (10^{14} @ 10 keV) X-ray beam exposure. Data processing was preformed using the IFEFFIT package. Rh and Co foils were used as standard references to calibrate energy shift and obtain passive electron reduction factor (S_0^2). It should be noted that the contributions from both metal and nonmetal (low-Z elements) neighbors were significant in the Rh spectra, which complicated the EXAFS analysis. Therefore, a similar method was adopted from ref. [30], with which the residuals of the fits to the metal contribution were separately fit to approximate the low-Z contribution. In addition, owing to the similarity of Rh–C and Rh–O EXAFS signals in the first nearest shell, they were treated as the Rh-low Z interactions. Based on ref. [30], the Rh–Rh(Co) and Rh-low Z interactions were analyzed with the phase shifts and back-scattering amplitudes obtained from the Feff calculations of Rh foil and Rh_2O_3 structures, respectively. Moreover, for the Rh_1Co_3 (Rh_1Co_1) bimetallic samples, the EXAFS spectra of both Rh K-edge and Co K-edge were fitted simultaneously with additional constraints[30] of coordination number (CN) relationship, bond length (R) and structure disordering (σ^2), i.e., $CN_{Rh-Co}/CN_{Co-Rh} = 3 : 1$ (or 1 : 1), $R_{Rh-Co} = R_{Co-Rh}$, $\sigma^2_{Rh-Co} = \sigma^2_{Co-Rh}$. For Co edge, the EXAFS signals were fitted based on the information of Co foil and CoO structures.

Catalytic performance evaluation. Tandem reactor experiments were carried out within two quartz tubes (7 mm ID, 9.6 mm OD) heated separately by two tandem furnaces (Thermo Scientific Lindberg/Blue M) under the atmospheric pressure. For a typical experiment, ~300 mg (Fe_3Ni_1/CeO_2) and ~200 mg (Rh_1Co_x/MCM-41, x = 0, 1, or 3) of catalysts (60–80 mesh) were loaded into the first and second flow reactors, respectively. Approximately 100 mg of acid-purified quartz particle

(60–80 mesh) was used for the dilution of each catalyst bed to reduce heat transport limitations. In prior to each reaction, the catalyst in the first reactor was pretreated under a mixture of H_2 and Ar (5/5 ml min^{-1}) at 600 °C for 1 h, during which process the catalyst in the second reactor was bypassed and maintained under Ar atmosphere. After the reduction, the catalyst bed in each reactor was heated to desired temperatures, and subsequently exposed to the reaction stream of C_2H_6/CO_2/Ar (6/3/3 ml min^{-1}) at the atmospheric pressure. The outlet of the first reactor was connected immediately to the inlet of the second reactor to ensure all the effluents enter into the second reactor. In addition, the outlet gasline of the second reactor was wrapped with heating tapes at 150 °C to avoid any condensations of water vapor and oxygenates. The exhaust was analyzed by an Agilent 7890B gas chromatography (PLOT Q and MOLESEIVE columns) equipped with a thermal conductivity detector and a flame ionized detector. Single reactor experiments followed the similar procedure. Water vapor was calibrated based on oxygen balance by running the reverse water-gas shift reaction with a PtCo/CeO_2 catalyst at different temperatures. The element balances of carbon, hydrogen, and oxygen were 100 ± 2%, 100 ± 3, and 100 ± 3%, respectively. Conversion (X), TOF, selectivity (S), and yield (Y) at steady state were calculated as follows:

$$X_i = \frac{[F_i]_{in} - [F_i]_{out}}{[F_i]_{out}} \times 100\% \quad (1)$$

$$TOF_i = \left| \frac{[F_i]_{in} - [F_i]_{out}}{CO\ uptake \cdot m_{catalyst}} \right| \quad (2)$$

where $[F_i]_{in}$ and $[F_i]_{out}$ referred to the inlet and outlet molar flow rate, respectively, of reactant i corrected by the Ar molar flow rate (mol min^{-1}); CO uptake (μmol g^{-1}) and $m_{catalyst}$ (mg) indicated the number of active site per unit mass of catalyst and the mass of catalyst, respectively.

The selectivity (S) of carbon containing species was defined separately for the first reactor, second reactor, and tandem reactor. For the first reactor (reaction of CO_2 and C_2H_6, C_2H_6-based selectivity),

$$S_i = \frac{[F_i]_{out}}{[F_{C_2H_6}]_{in} - [F_{C_2H_6}]_{out}} \times \frac{n_{carbon-atoms,i}}{n_{carbon-atoms,C_2H_6}} \times 100\% \quad (3)$$

where the species i could be CO, CH_4, C_2H_4, C_3H_6, C_3H_8, C_4H_8, C_4H_{10}; n is the number of carbon from C_2H_6 in species i. It should be noted that the CO reported here is the part produced from C_2H_6 via dry reforming reaction. Based on the oxygen balance, S_{CO} was calculated in the following:

$$S_{CO} = \frac{([F_{CO}]_{out}) - [F_{H_2O}]_{out}/2}{[F_{C_2H_6}]_{in} - [F_{C_2H_6}]_{out}} \times \frac{n_{carbon-atoms,CO}}{n_{carbon-atoms,C_2H_6}} \times 100\% \quad (4)$$

For the second reactor (reaction of C_2H_4, CO, and H_2, C_2H_4-based selectivity),

$$S_i = \frac{[F_i]_{out}}{[F_{C_2H_4}]_{in} - [F_{C_2H_6}]_{out}} \times \frac{n_{carbon-atoms,i}}{n_{carbon-atoms,C_2H_4}} \times 100\% \quad (5)$$

where the species i could be C_2H_6, C_3H_6, C_3H_8, C_4H_8, C_4H_{10}, C_3H_6O (propanal) and C_3H_8O (1-propanol); n is the number of carbon from C_2H_4 in species i. Note: n should be 2 for C_3H_6O and C_3H_8O.

For the tandem reactor, it follows the same definition as that of the first reactor with a C_2H_6-based selectivity. Species i could be CO, CH_4, C_2H_4, C_3H_6, C_3H_8, C_4H_8, C_4H_{10}, C_3H_6O (propanal) and C_3H_8O (1-propanol). Note: n was chosen as 3 for C_3H_6O and C_3H_8O.

The yield (Y) of carbon containing species was the product of conversion and selectivity, i.e.,

$$Y_i = X_i \cdot S_i \quad (6)$$

Density functional theory calculation methods. Spin polarized periodic DFT[31,32] calculations were performed using Vienna Ab-Initio Simulation Package (VASP) code[33,34]. Projector augmented wave potentials were used to describe the core electrons with the generalized gradient approximation[35,36], using PW91 functionals[37]. The Kohn–Sham one-electron wave functions were expanded by using a plane wave basis set with a kinetic energy cutoff of 400 eV. The Brillouin zone was sampled using a $3 \times 3 \times 1$ k-point grid in the Monkhorst–Pack scheme[38].

The Rh(111) surface was modeled using a four layer 4×4 surface slab. The bulk-terminated $Co_3Rh(111)$ surface was cleaved using a L_{12}-Co_3Rh cubic crystal structure. A 15 Å thick vacuum was added along the direction perpendicular to the surface in the initial slab model to avoid the artificial interactions between the slab and its periodic images. During geometry optimization, the atoms in the top two layers were allowed to relax while the atoms in the bottom two layers were fixed. Ionic positions were optimized until Hellman-Feynman force on each ion was smaller than 0.02 eV/Å.

The binding energy (BE) of an adsorbate is calculated as:

$$BE_{adsorbate} = E_{slab+adsorbate} - E_{slab} - E_{adsorbate} \quad (7)$$

where $E_{slab+adsorbate}$, E_{slab}, and $E_{adsorbate}$ are the total energies of slab with adsorbate, clean slab, and adsorbate species in gas phase, respectively.

The transition state of a chemical reaction was located using the climbing image nudged elastic band method implemented in VASP[39]. The activation energy (E_a) of a chemical reaction is defined as the energy difference between the initial and transition states.

Data availability

References

1. Rekker, S. A., O'Brien, K. R., Humphrey, J. E. & Pascale, A. C. Comparing extraction rates of fossil fuel producers against global climate goals. *Nat. Clim. Change* **8**, 489–492 (2018).
2. Rogelj, J., Forster, P. M., Kriegler, E., Smith, C. J. & Séférian, R. Estimating and tracking the remaining carbon budget for stringent climate targets. *Nature* **571**, 335–342 (2019).
3. Turner, P. A., Field, C., Lobell, D. B., Sanchez, D. & Mach, K. Unprecedented rates of land-use transformation in modelled climate change mitigation pathways. *Nat. Sustain* **1**, 240–245 (2018).
4. Thomas, M., Partridge, T., Harthorn, B. H. & Pidgeon, N. Deliberating the perceived risks, benefits, and societal implications of shale gas and oil extraction by hydraulic fracturing in the US and UK. *Nat. Energy* **2**, 1–7 (2017).
5. Boudet, H. S. Public perceptions of and responses to new energy technologies. *Nat. Energy* **4**, 446–455 (2019).
6. Yan, B. et al. Active sites for tandem reactions of CO_2 reduction and ethane dehydrogenation. *Proc. Natl Acad. Sci. USA* **115**, 8278–8283 (2018).
7. Gomez, E. et al. Combining CO_2 reduction with propane oxidative dehydrogenation over bimetallic catalysts. *Nat. Commun.* **9**, 1–6 (2018).
8. Xie, Z. et al. Effects of oxide supports on the CO_2 reforming of ethane over Pt-Ni bimetallic catalysts. *Appl. Catal. B. Environ.* **245**, 376–388 (2019).
9. Sullivan, M. M. & Bhan, A. Effects of oxygen coverage on rates and selectivity of propane-CO_2 reactions on molybdenum carbide. *J. Catal.* **357**, 195–205 (2018).
10. Zhang, R. et al. Photocatalytic oxidative dehydrogenation of ethane using CO_2 as a soft oxidant over Pd/TiO2 catalysts to C_2H_4 and syngas. *ACS Catal.* **8**, 9280–9286 (2018).
11. Porosoff, M. D. et al. Identifying different types of catalysts for CO_2 reduction by ethane through dry reforming and oxidative dehydrogenation. *Angew. Chem. Int. Ed.* **54**, 15501–15505 (2015).
12. Nowicka, E. et al. Elucidating the role of CO_2 in the soft oxidative dehydrogenation of propane over ceria-based catalysts. *ACS Catal.* **8**, 3454–3468 (2018).
13. Ramirez, A. et al. Effect of zeolite topology and reactor configuration on the direct conversion of CO_2 to light olefins and aromatics. *ACS Catal.* **9**, 6320–6334 (2019).
14. Gomez, E., Nie, X., Lee, J. H., Xie, Z. & Chen, J. G. Tandem reactions of CO_2 reduction and ethane aromatization. *J. Am. Chem. Soc.* **141**, 17771–17782 (2019).
15. Market Research Future. *Aldehyde Market Research Report-Global Forecast Till 2025.* https://www.marketresearchfuture.com/reports/aldehyde-market-2356 (2019).
16. Market Research Future. *Industrial Alcohol Market Research Report-Forecast to 2023.* https://www.marketresearchfuture.com/reports/industrial-alcohol-market-5787 (2019).
17. Cornils, B., Herrmann, W. A. & Rasch, M. Otto Roelen, pioneer in industrial homogeneous catalysis. *Angew. Chem. Int. Ed.* **33**, 2144–2163 (1994).
18. Dingwall, P. et al. Understanding a hydroformylation catalyst that produces branched aldehydes from alkyl alkenes. *J. Am. Chem. Soc.* **139**, 15921–15932 (2017).
19. Pandey, S. et al. Iron catalyzed hydroformylation of alkenes under mild conditions: evidence of an Fe(II) catalyzed process. *J. Am. Chem. Soc.* **140**, 4430–4439 (2018).
20. Iu, L., Fuentes, J. A., Janka, M. E., Fontenot, K. J. & Clarke, M. L. High iso aldehyde selectivity in the hydroformylation of short-chain alkenes. *Angew. Chem. Int. Ed.* **58**, 2120–2124 (2019).
21. Börner A, Franke R. *Hydroformylation: fundamentals, processes, and applications in organic synthesis* (John Wiley & Sons, 2016).
22. Franke, R., Selent, D. & Börner, A. Applied hydroformylation. *Chem. Rev.* **112**, 5675–5732 (2012).
23. Grant, J. T. et al. Selective oxidative dehydrogenation of propane to propene using boron nitride catalysts. *Science* **354**, 1570–1573 (2016).
24. Gao, Y. et al. Recent advances in intensified ethylene production—a review. *ACS Catal.* **9**, 8592–8621 (2019).
25. Wang, L. et al. Atomic-level insights in optimizing reaction paths for hydroformylation reaction over Rh/CoO single-atom catalyst. *Nat. Commun.* **7**, 1–8 (2016).
26. Lang, R. et al. Hydroformylation of olefins by a rhodium single-atom catalyst with activity comparable to RhCl (PPh3)3. *Angew. Chem. Int. Ed.* **55**, 16054–16058 (2016).
27. Yates, J. Jr., Duncan, T., Worley, S. & Vaughan, R. Infrared spectra of chemisorbed CO on Rh. *J. Chem. Phys.* **70**, 1219–1224 (1979).
28. Rice, C., Worley, S., Curtis, C., Guin, J. & Tarrer, A. The oxidation state of dispersed Rh on Al2O3. *J. Chem. Phys.* **74**, 6487–6497 (1981).
29. Ciuparu, D. et al. Mechanism of cobalt cluster size control in Co-MCM-41 during single-wall carbon nanotubes synthesis by CO disproportionation. *J. Phys. Chem. B* **108**, 15565–15571 (2004).
30. Frenkel, A. I. Applications of extended X-ray absorption fine-structure spectroscopy to studies of bimetallic nanoparticle catalysts. *Chem. Soc. Rev.* **41**, 8163–8178 (2012).
31. Hohenberg, P. & Kohn, W. Inhomogeneous electron gas. *Phys. Rev.* **136**, B864 (1964).
32. Kohn, W. & Sham, L. J. Self-consistent equations including exchange and correlation effects. *Phys. Rev.* **140**, A1133–A1138 (1965).
33. Kresse, G. & Furthmüller, J. Efficiency of ab-initio total energy calculations for metals and semiconductors using a plane-wave basis set. *Comp. Mater. Sci.* **6**, 15–50 (1996).
34. Kresse, G. & Hafner, J. Ab initio. *Phys. Rev. B* **48**, 13115–13118 (1993).
35. Blöchl, P. E. Projector augmented-wave method. *Phys. Rev. B* **50**, 17953–17979 (1994).
36. Kresse, G. & Joubert, D. From ultrasoft pseudopotentials to the projector augmented-wave method. *Phys. Rev. B* **59**, 1758–1775 (1999).
37. Perdew, J. P. & Wang, Y. Pair-distribution function and its coupling-constant average for the spin-polarized electron gas. *Phys. Rev. B* **46**, 12947–12954 (1992).
38. Monkhorst, H. J. & Pack, J. D. Special points for Brillouin-zone integrations. *Phys. Rev. B* **13**, 5188–5192 (1976).
39. Henkelman, G. A climbing image nudged elastic band method for finding saddle points and minimum energy paths. *J. Chem. Phys.* **113**, 9901–9904 (2000).

Acknowledgements

Author contributions

Z.X., Y.X., and M.X. contributed equally to this work. Z.X., Y.X., M.X., and J.G.C. designed the experiments. Z.X. synthesized the catalysts and carried out the characterizations and catalytic performance evaluations. Z.X., Y.X., M.X., and E.S. conducted the synchrotron experiments. X.C. performed the TEM and STEM imaging. Z.X. and J.H.L analyzed the XAFS data. S.K. conducted the DFT calculations. Z.X., S.K., and J.G.C. wrote the paper and J.G.C. supervised the whole project.

Competing interests

The authors declare no competing interests.

Additional information

Supplementary information is available for this paper at https://doi.org/10.1038/s41467-020-15849-x.

Correspondence and requests for materials should be addressed to S.K. or J.G.C.

Peer review information *Nature Communications* thanks Anne M. Gaffney and the other, anonymous, reviewer(s) for their contribution to the peer review of this work.

Reprints and permission information is available at http://www.nature.com/reprints

Publisher's note Springer Nature remains neutral with regard to jurisdictional claims in published maps and institutional affiliations.